International Journal of Thermophysics, Vol. 28, No. 4, August 2007 (© 2007)
DOI: 10.1007/s10765-007-0174-2

On the Optical, Thermal, and Vibrational Properties of Nano-ZnO:Mn, A Diluted Magnetic Semiconductor

P. Vinotha Boorana Lakshmi[1] **and K. Ramachandran**[1,2]

Received February 13, 2006

Nano-zinc oxide and Mn-doped zinc oxide were synthesized by a chemical process, and the average size of the particles observed was 35 nm for nano-ZnO. Optical and thermal characterizations were carried out by means of photoluminescence and photoacoustic spectroscopy. It was found that nano-ZnO has a thermal diffusivity one order of magnitude larger than bulk ZnO. Similarly, a less explored localized defect mode in ZnO:Mn was studied theoretically and experimentally using FTIR spectroscopy. The localized mode was experimentally found to be 514 cm^{-1}, compared to its theoretical value of 502 cm^{-1}. These values suggest that the current theory of bulk materials can also be extended to nanosystems and they are consistent with our hypothesis that Mn goes substitutionally as an impurity displacing Zn in nano-ZnO.

KEY WORDS: localized vibrational mode (LVM); photoacoustics; thermal diffusivity; thermal conductivity; ZnO; ZnO:Mn nanocrystals.
PACS: 63.20.pw, 78.66.Hf, 33.20.Ea

1. INTRODUCTION

Zinc oxide (ZnO), a hexagonal wurtzite crystal, is a promising material for manufacturing photodetectors, blue and ultraviolet laser diodes [1], transparent field effect transistors, etc. and has gained attention because of its electronic properties, i.e., a direct bandgap semiconductor with $E_g = 3.3$ eV and a large exciton binding energy of 60 meV. Diluted magnetic semiconductors (DMS) (semiconductors doped with a small concentration of magnetic impurities) are promising materials for spintronics devices.

[1] School of Physics, Madurai Kamaraj University, Madurai 625 021, India.
[2] To whom correspondence should be addressed. E-mail: thirumalchandran@yahoo.com

0195-928X/07/0800-1353/0 © 2007 Springer Science+Business Media, LLC

In recent years, due to the prediction of a possible ferromagnetic transition in metal-doped ZnO with a Curie temperature above room temperature, research on ZnO:Mn has increased significantly [2]. The theory proposed by Dietl [3] predicts room temperature ferromagnetism in Mn-doped p-type ZnO. In addition to Dietl's prediction, ferromagnetism (FM) in magnetically doped ZnO has been theoretically investigated by *ab initio* calculations based on the local density approximation [2]. Although reviews are available for bulk and nano-ZnO doped with magnetic impurities like Co and V [4], very few reports are available for ZnO doped with manganese [5]. Sharma et al. [2] have carried out measurements on ZnO:Mn for the FM transition. Since the optical and thermal properties are enhanced by, at least, a few orders of magnitude in nano-ZnO, studies on nano-ZnO:Mn have become important. Recently it has been reported [6] that Mn doping in ZnO even at a low level (of 2 at.%) can change the bandgap of the ZnO host, and this change is not due to experimental uncertainty. This is a very important issue since then the localized mode due to doping can also change the observed physical properties.

Although ZnO:Mn is a potential DMS material for many devices and there are other interesting properties like the FM transition, etc., to date studies on the defect mode in this material have not been given much attention. Here this gap is filled. A practical challenge in the synthesis of the DMS nanostructure is to incorporate the dopant into the ZnO. Very little work has been reported for changes in the local structure and vibrational properties of the Mn-doped ZnO [7], and to our knowledge no theoretical results have yet been reported for the vibrational modes.

The impurities, introduced into the ZnO nanostructure, can modulate the local structure and cause a dramatic change of photoelectric and vibrational properties due to the quantum confinement effect [8–11]. Therefore, ZnO:Mn is studied here with an emphasis on the local defect mode.

Recently, numerous experiments have been performed on the synthesis and optical properties of one-dimensional (1D) nanostructured ZnO [12–16], including Mn doping, and Gebicki et al. [17] have experimentally synthesized bulk ZnO:Mn and characterized it by using XRD and Raman spectroscopy and reported a mode at about 470 cm^{-1} as the localized vibrational mode (LVM). Since to the best of our knowledge theoretical studies on ZnO:Mn for LVM are not available even for bulk, an attempt is made here to study the LVM of ZnO:Mn by both experiment and theory along with its optical and thermal properties.

2. EXPERIMENT

2.1. Synthesis

There are two widely accepted chemical routes for the synthesis: through zinc acetate and zinc sulphate. Here the zinc sulphate route is chosen for the synthesis and ZnO nanocrystals are synthesized through two-step solid-state reactions as follows:

(1) Anhydrous zinc sulphate and sodium carbonate were taken in an equimolar ratio and mixed and ground properly for 30 min in a very clean mortar where dry flake-like particles were formed.

(2) Since the reaction temperature is very important for the growth of nanoparticles, the above mixture is heated in a furnace for 1 h at a temperature of 200 °C. The powder was collected and then it is cleaned three times with distilled water and washed twice with pure ethanol. Again this is dried at 80 °C to form ZnO powder so that it is free from the hydroxyl group

$$ZnSO_4 \cdot 7H_2O + Na_2CO_3 \rightarrow ZnO + Na_2SO_4 + CO_2 + 7H_2O.$$

Similarly the manganese dioxide nanoparticles are formed by grinding the manganese dioxide powder for 30 min and through the same heating and washing process as for the preparation of ZnO nanoparticles, MnO_2 nanoparticles were obtained.

The nanoparticles of zinc oxide doped with manganese are prepared by mixing the zinc oxide and manganese dioxide nanoparticles in 80:20 mol.% ratio, which is taken as the initial charge and when the process is repeated (heating to 200 °C and washing, etc.), we obtain ZnO nanoparticles doped with manganese. Confirmation is carried out by making XRD measurements.

2.2. X-Ray Diffraction

The ZnO nanoparticles have been structurally characterized by X-ray diffraction (XRD, MAC Science, MXP18) with CuK_α radiation. The XRD pattern of ZnO nanoparticles reveals a wurtzite structure. The lattice constants of the ZnO nanocrystal are $a = b = 3.27$ Å and $c = 5.21$ Å. A typical XRD pattern of the nanocrystal is shown in Fig. 1. There are three main peaks at (100), (002), and (001). Moreover, the relative peak intensity of (100) to (002) in the present case is quite different from that reported by Pan et al. [14] implying that ZnO nanocrystals prepared by various methods may exhibit different preferred growth orientations. The

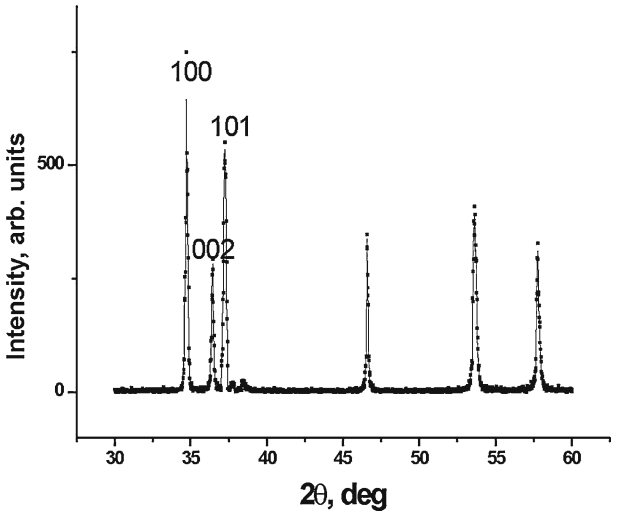

Fig. 1. XRD pattern of ZnO nanocrystal.

size of the particles is determined by using Scherrer's formula as a first approximation.

2.3. Photoluminescence

Photoluminescence emission spectra of the ZnO nanocrystal are recorded using a spectroflurophotometer (Shimadzu RF-5000) at room temperature. Here we obtained an emission peak at $\lambda = 380\,\text{nm}$ (Fig. 2) which corresponds to the characteristic excitation peak of ZnO, while the visible green emission at 510 nm is believed to arise from the defect levels associated with oxygen vacancies or zinc interstitials, which agrees well with the spectrum obtained by Lee [18]. A similar spectrum for a very diluted Mn concentration in ZnO shows the same trend.

2.4. Photoacoustic Spectroscopy (PAS)

The photoacoustic technique is used to characterize several semiconductors because of its great versatility as a non-destructive and non-invasive method for evaluation of materials. Since Scherrer's formula used to find the size of the particles from an X-ray photograph is not exact, it is used only as a guideline for further measurement. Thus, photoacoustic measurements are used here to determine the size of the particle.

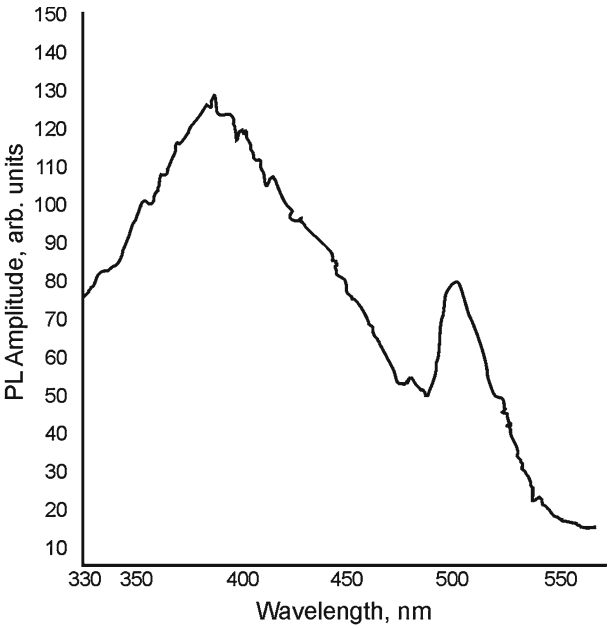

Fig. 2. PL spectrum of ZnO nanocrystal.

When a modulated light is absorbed by the sample located in a sealed cell, the non-radiative decay of the absorbed light produces a modulated transfer of heat to the surface of the sample. This modulated thermal gradient produces pressure waves in the gas inside the cell that can be detected by the microphone attached to the cell. The resulting signal depends not only on the amount of heat generated in the sample (and, hence, on the optical absorption coefficient and the light-to-heat conversion efficiency of the sample), but also on how the heat diffuses through the sample [19]. The quantity, which describes the rate of heat diffusion in a material, is the thermal diffusivity α. Thus, photoacoustic measurements are used not only to characterize the nanomaterial but also to measure certain thermal and optical properties.

2.4.1. Photoacoustic Spectrometer

The light from a 400 W Xe-lamp (Jobin Yvon) is mechanically chopped by an electro-mechanical chopper (PAR Model 650) and focused onto the sample through a monochromator (Triax Model 180, Jobin Yvon). The sample is placed in the PA cell, and a microphone is placed very near the sample. The PA signal from the microphone is fed to a

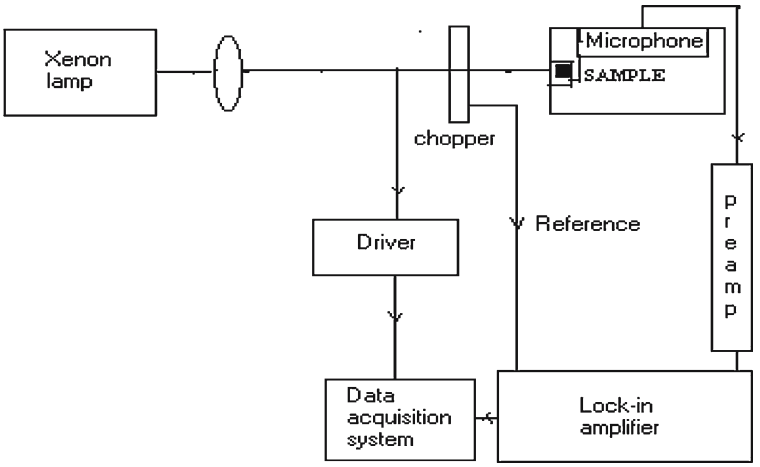

Fig. 3. Photoacoutic spectrometer.

lock-in amplifier (Perkin Elmer Model 7225 DSP) for further measurements, and this PA experimental setup is shown in Fig. 3.

2.4.2. Photoacoustic Measurements

2.4.2.1. Depth Profile Analysis. A ZnO nanocrystal is placed inside the PA cell, and the PA signal is observed for different chopping frequencies. The thermal diffusivity was determined from the thermal diffusion model [20] of the photoacoustic effect which states that, for an optically opaque and thermally thin sample, the pressure fluctuations are given by

$$\delta p = \gamma\, p_0 I_0 \left(\alpha_g \alpha_s\right)^{1/2} \exp j\left(\omega t - \frac{\pi}{2}\right) / 2\pi\, T_0 l_g \kappa_s f \sinh\left(l_s \sigma_s\right), \tag{1}$$

where γ is the specific heat ratio of air, p_0 is the ambient pressure, I_0 is the incident light beam intensity, T_0 is the room temperature, f is the chopping frequency, and l_i, k_i, and α_i are the thickness, thermal conductivity, and thermal diffusivity of material i, respectively.

The subscript i denotes either sample (s) or gas (g) and $\sigma_i = (1+j)\, a_i$ with $a_i = (\pi f/\alpha_i)^{1/2}$ is the complex thermal diffusion coefficient of material "i". Particularly, for an optically opaque and thermally thick sample ($l_s \sigma_s \gg 1$), the expression for the photoacoustic amplitude is given by

$$S = \frac{A}{f} \exp(-a f^{1/2}), \tag{2}$$

where the constant A, apart from geometric constants, includes factors such as the light intensity, room temperature, gas thermal properties, and

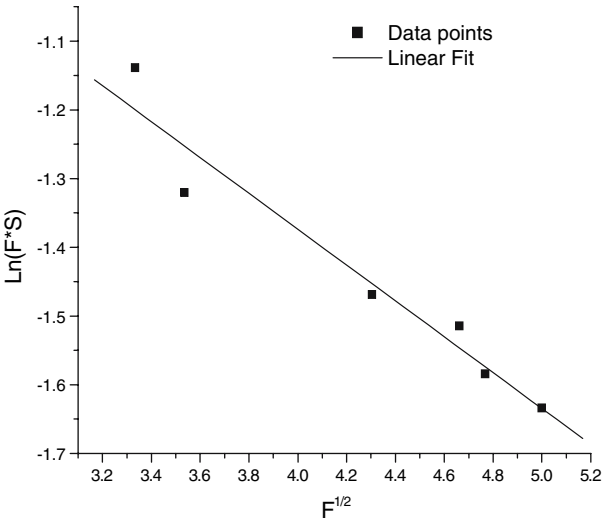

Fig. 4. Depth profile of ZnO nanocrystal.

$a = \left(\pi l_s^2/\alpha_s\right)^{1/2}$. From the slope of $\ln(fS)$ as a function of $\sqrt{f}$, we deduce the thermal diffusivity, α, of the sample from this relation $a = \left(\pi l_s^2/\alpha_s\right)^{1/2}$. This is shown in Fig. 4, where the data are fitted for best straight line (by least squares) and the slope of the line is used to deduce the thermal diffusivity. The possibility of scattering of data points around a straight line exists for discontinuous atomic structures. This is not seen in crystals where continuous arrangement of atoms in certain periodicity exists. But here the situation is different with agglomeration of nanoparticles. Connectivity between particles is the result of pelletization. If more pressure is applied in this pelletization process, then one can reduce the non-linearity in the data points because the resulting structure becomes more homogeneous. In all the photoacoustic measurements, the nanoparticles of ZnO were not used, as obtained from the chemical reaction. The powders were collected and palletized. Depending on the pressure applied during pelletization, the connectivity of the particles is achieved and can be measured by the degree of departure from a straight line as shown in Fig. 4.

We prepared the pellet by applying a pressure of about 1 ton. We have also synthesized nano-cadmium sulphide where the effect of pressure on the size of the particle and thermal conductivity have been studied [21]. The size of the particles affects the PA frequency response and hence the thermal properties. The foregoing discussion is also valid in this case. In

summary, what we deduce is only an average value of the thermal diffusivity.

The thermal conductivity is given by

$$\kappa = \alpha \rho C_p \ [\mathrm{W \cdot m^{-1} \cdot K^{-1}}], \tag{3}$$

where ρ is the density and C_p is the specific heat capacity.

The thermal diffusivity of the zinc oxide nanocrystal is found to be $1.7 \times 10^{-5}\,\mathrm{m^2 \cdot s^{-1}}$ and is compared with the thermal diffusivity of the ZnO nanowire which is $7.15 \times 10^{-5}\ \mathrm{m^2 \cdot s^{-1}}$ [22], whereas that for bulk ZnO is $7.1 \times 10^{-6}\,\mathrm{m^2 \cdot s^{-1}}$ [23] and the thermal conductivity of the nanocrystals is $50.16\,\mathrm{W \cdot m^{-1} \cdot K^{-1}}$. The thermal diffusivity and thermal conductivity of the nanocrystal are at least one order of magnitude higher than that for bulk ZnO [22]. The thermal diffusivity of the nanoparticles will be enhanced when compared with the bulk system because at this size of the particles, quantum confinement is achieved and the interface will form an extremely dense network of paths for fast diffusion through the nanocrystals. In general, the material properties will be enhanced as the size of the particles decrease, due to quantum confinement [24] in nanomaterials. But in nanowires and nanobelts, many reports are available [25] that show a decrease in thermal conductivity and thermal diffusivity, when the particle size is reduced. In nanowires, the thickness plays an important role. For example, in nano-ZnSe [26], it has been found that if the thickness is more than 10 nm, then there is a possibility for agglomeration of the nanoparticles on the surface of the wires, forming clusters which will lead to multiple scattering and a reduction in the thermal conductivity compared to the bulk value, whereas when the thickness is between 5 and 10 nm, the reverse occurs. Similarly in these films, the surface of which contains 50% of the nanoparticles, there will only be a reduction in thermal properties. This has also been observed in ZnO thin films [27]. However, when nanopowders of ZnO are considered (isolated particles), the defect concentration is lower compared to nanowires or thin films. Therefore, a marginal increase in thermal properties is possible. But when compared with ZnO nanowires, the thermal diffusivity and thermal conductivity for nanoparticles are less, and this is discussed in the next section after determining the size of the particles.

2.4.2.2. Wavelength Scanning. The detected photoacoustic power is proportional to the absorption of optical energy by the sample. The PA spectrum was obtained by recording the PA signal as a function of the wavelength of the incident beam, for a constant modulation frequency. The PA spectrum for each sample is normalized using the PA spectrum

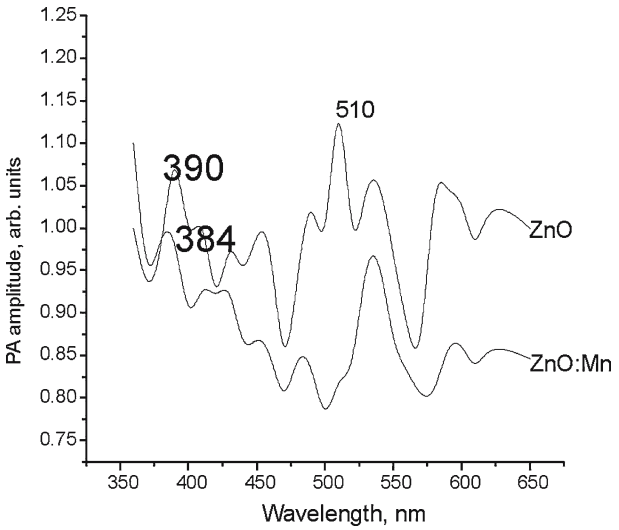

Fig. 5. PA spectrum of undoped and Mn doped ZnO nanocrystal.

obtained for carbon black. This is essential as the power spectrum of the light source (xenon lamp) is simply the PA spectrum for photoacoustically opaque samples. The PA spectra of ZnO and ZnO:Mn are given in Fig. 5.

Here, two prominent peaks are observed at 390 and 520 nm, and they are identified as due to bandgap absorption and oxygen related impurities, i.e., the peak positioned at 390 nm corresponds to the zinc oxide exciton peak while the peak at 510 nm corresponds to the emission originating from intrinsic defects in ZnO, such as oxygen vacancies, donor acceptor complexes, and anti-site oxygen [18] and for nano-ZnO:Mn the peak occurs at 384 nm and a shoulder occurs at 510 nm.

In general, it is expected that for a nanomaterial the bandgap should show a blue shift compared to the bulk. But, here 390 nm for the bandgap excitation is red shifted. This is possible in nanomaterials, when excess Zn atoms are collected in ZnO nanomaterials.

Similarly when ZnO is doped with Mn, the bandgap is shifted from 390 nm to 384 nm. Since doping will not change the bandgap, the experiment is repeated a few times so that experimental uncertainties can be minimized. The value is still 384 nm which indicates that Mn doping can change the bandgap. As already mentioned, Ranjani et al. [6] have recently reported a similar result in ZnO:Mn nanocrystals and finally concluded that for nanomaterials when magnetic materials are used as dopants, there is a possibility for a change in the bandgap due to exchange interactions.

Table I. Bandgap Values of Bulk and Nano-ZnO

System	Bandgap (eV)	Reference
Bulk ZnO	3.3	[28]
Nano-ZnO (35 nm)	3.18	Present work
Nano-ZnO:Mn	3.26	Present work

Error in measurements ~2%.

Because of the inclusion of the manganese into the zinc oxide, the exciton peak of the ZnO exhibits a blue shift and the intensity of the peaks, which arises due to the oxygen vacancies or zinc interstitials, is also reduced. The bandgaps obtained from the present measurements are given in Table I along with the bulk values.

From the bandgap, the particle size of the ZnO nanoparticle was found from the following expression [29]:

$$E_{\mathrm{gn}} = \left[E_{\mathrm{gb}}^2 + \left\{ \frac{2h^2 E_{\mathrm{gb}} \left(\frac{\pi}{R}\right)^2}{m^*} \right\} \right]^{1/2}, \tag{4}$$

where E_{gb} is the bandgap of the bulk semiconductor (3.3 eV for ZnO), R is the particle radius, m^* is the effective mass of the electron ($0.3\,m_e$), and E_{gn} is the bandgap for the nanosystem. The average particle size of the ZnO nanocrystals here is found to be 35 nm, and this is of the same order as reported in Ref. [30]. Since the particle size is around 35 nm, the enhancement in the observed thermal diffusivity is just one order of magnitude. Still the size can be reduced.

The other interesting optical property, namely, the defect vibrational mode, due to doping has to be analyzed as there is an appreciable change in electronic behavior, i.e., a change in the bandgap. The size of the observed particle when we synthesized ZnO nanowire is 20 nm (in diameter) and the length is 100 nm. This is still smaller compared to 35 nm sized particles now synthesized. This explains why in the present case the thermal diffusivity is lower than that for the nanowire.

2.5. FTIR Spectrum

IR spectra are recorded for nano-ZnO and ZnO:Mn systems to analyze the changes in the vibrational modes, as given in the introduction. Wurtzite ZnO belongs to the $C6v4$ space group ($P63mc$). At the Γ point of the Brillouin zone, the normal vibrational modes are predicted on the

basis of group theory $\Gamma_{\text{opt}} = A_1 + 2B_1 + E_1 + 2E_2$ [9,10,31,32]. Among these, E_1 and A_1 are infrared active.

Infrared spectra were obtained using the Perkin–Elmer spectrometer to study the vibrational modes for nano-ZnO and manganese-doped ZnO which are shown in Fig. 6. The modes observed for undoped ZnO at 379.95 cm^{-1}, 416.60 cm^{-1} agree well with the already reported values of bulk ZnO [33] corresponding to the A_1 and E_1 species which are again observed in ZnO:Mn. But ZnO:Mn exhibits an additional mode at 514 cm^{-1} which agrees very well with the ZnO:Mn tetrapod [7] reported earlier, and this additional mode at 514 cm^{-1} needs study. A theoretical investigation is carried out to explain the defect mode.

3. THEORETICAL STUDY

The localized vibrational modes are studied for ZnO:Mn theoretically by using a molecular model and the Green function.

3.1. Molecular Model

This model as developed by Jaswal [34], is employed here to study the LVM of ZnO:Mn; the details are not reported here. Only a few important steps are given here. To start with, it is assumed that Mn substitutes for the Zn site as shown in Fig. 7. Then the four neighboring atoms with $l = 2$–5 are the neighbors with atomic positions ($1/2\,1/2\,1/2$), ($1/2\,1/2\,1/2$), ($1/2\,1/2\,1/2$), and ($1/2\,1/2\,1/2$). The second neighbor interactions are neglected.

Nearest neighbor interactions are given in terms of the two Kellermann's parameters A and B as

$$\frac{1}{r}\left[\frac{dV}{dr}\right]\Bigg|_{r=r_0} = \frac{e^2}{2v}B \tag{5}$$

$$\frac{d^2V}{dr^2}\Bigg|_{r=r_0} = \frac{e^2}{2v}A \tag{6}$$

where V is the short-range potential for the first neighbor interactions and v is the volume of the unit cell. Similarly, when the defect is introduced, these interactions will be modified as A' and B'. Now V_1 is the interaction potential between the defect atom and its neighbors.

The relevant data on the elastic constants and the effective charge for ZnO can be obtained from the literature [5] for the calculation of A and

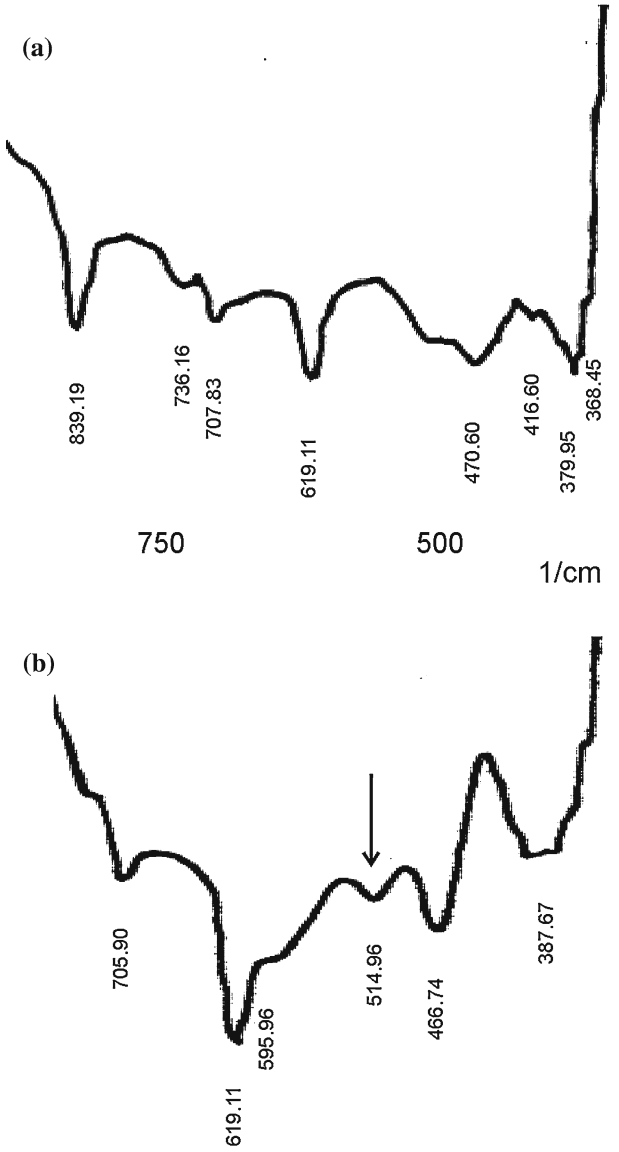

Fig. 6. FTIR spectrum of (a) ZnO and (b) ZnO:Mn nanocrystal. Arrow indicates the LVM due to Mn doping.

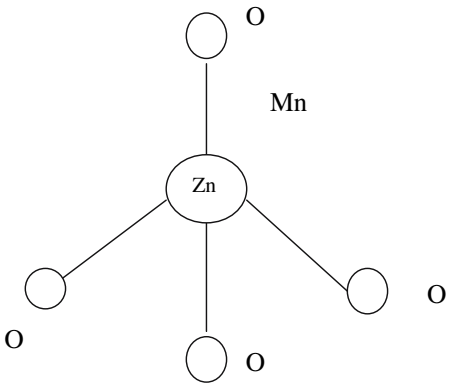

Fig. 7. T_d symmetry of the molecule ZnO:Mn.

B. The equations of motion of the atoms in the molecule in the defect environment can now be written as

$$m_l \ddot{u}_\alpha (l) = -\sum_{l' \ \beta} \Phi_{\alpha\beta} (ll') u_\beta (l') \tag{7}$$

where l and l' are from 1 to 5. Assuming harmonic solutions for the equations of motion, and the fact that $\Phi_{\alpha\beta}$ is a sum of $\Phi^{C}_{\alpha\beta} + \Phi^{R}_{\alpha\beta}$ where $\Phi^{C}_{\alpha\beta}$ corresponds to the second derivative of the Coulomb potential with respect to the displacement components of the atoms, and $\Phi^{R}_{\alpha\beta}$ is a similar derivative of the short-range potential between the nearest neighbors defined through A and B or A' and B'. In brief, the dynamical matrix is constructed taking into account the long- and short-range interactions of the nearest neighbors.

The dynamical matrix is given by

$$D_{\alpha\beta}(l - l') = D^{C}_{\alpha\beta}(ll') + D^{R}_{\alpha\beta}(ll'), \tag{8}$$

where $D^{C}_{\alpha\beta}$ is the coupling coefficient corresponding to the Coulomb potential and $D^{R}_{\alpha\beta}$ is the coupling coefficient corresponding to the short-range potential ($\Phi_{\alpha\beta}$) between the nearest neighbors, defined through the force constants A and B. $D^{C}_{\alpha\beta}$ and $D^{R}_{\alpha\beta}$ are determined following the usual procedures.

When the interactions are limited to nearest neighbors, the dynamical matrix will be of order 15×15 as there are five atoms in this molecule. This dynamical matrix is diagonalized to get the eigen-frequencies

Table II. Rigid Ion Model Parameters for ZnO (All parameters are in units of N·cm^{-1}, except for Z which is an effective charge, a number.)

A	B	C_1	D_1	E_1	F_1	C_2	D_2	E_2	F_2	Z
−0.445	−0.30	−0.12	−0.54	0	−0.144	−0.08	0.115	0.0	0.005	0.065

Table III. LVM Using Different Techniques for ZnO:Mn

Technique	LVM (cm^{-1})	Reference
Green Function	502.2	Present
Molecular model	463.5	Present
Experiment	470.0	[4]
	522.0	[10]
	514.9	Present

and eigenvectors, and the defect mode is identified from the eigenvector, as usual. The Kellerman parameters determined by the rigid ion model are given in Table II. A program is written and executed to find the localized mode. This is given in Table III.

3.2. Green-Function Formalism

Since in the molecular model, only central forces are considered and only for first neighbors, we carried out Green's function calculations also to find the LVM, where second neighbors and non-central forces are considered. The Green-function technique developed by Maradudin et al. [35] is effective in explaining the defect modes in crystals and is followed here.

When a substitutional impurity is added to a host system, the modes will be altered and the defect modes are evaluated from $|I - g\partial l| = 0$ where I is the identity matrix, g is the green function matrix of the host system, and ∂l is the perturbation matrix associated with the substitutional impurity added to the host system. The Green function is a complex quantity where the real part is useful in the study of impurity vibrations and the imaginary part in evaluating the frequency spectrum of the host system.

The Green function is evaluated from

$$g_{\alpha\beta}\begin{pmatrix} 0 & l \\ k & k' \end{pmatrix} = \frac{1}{N}\sum_{qj} \frac{e_\alpha(k|qj)\, e^*_\beta(k'|qj)}{(x^2 - x_j^2(q))} \cos\left(2\pi \bar{q}\cdot\bar{r}\begin{pmatrix} 0 & l \\ k & k' \end{pmatrix}\right), \qquad (9)$$

where $x = \omega/\omega_{\max}$ and $x_j(q) = \omega_j(q)/\omega_{\max,}$ $\omega_{\max}$ being the maximum allowed frequency of the host lattice. N is the number of unit cells in the crystal and $e(k|qj)$ are the eigenvectors.

To start with, the Green functions for the ZnO host system are evaluated from the phonons and eigenvectors, which are computed from the refined rigid ion model developed by Plumelle and Vandevyver [36].

The Green function matrix for the host ZnO in the defect space is of the order 15×15. The reduced matrices g and ∂l are sufficient to determine the LVMs in the case of ZnO:Mn for the calculation corresponding to T_d symmetry of the defect complex. This is obtained from group theoretical simplifications as $\Gamma_{15} = A_1 + E + F_1 + 3F_2$. The block diagonalized matrix of g and ∂l for ZnO:Mn for F_2 has been reported in an earlier paper [37].

The perturbation matrix ∂l due to the substitutional impurity is written as

$$\partial l_{\alpha\beta}\left(k, k'\right) = \varepsilon M_k \omega^2 \delta_{\alpha\beta}\delta_{kk'} - \Delta\phi_{\alpha\beta}\left(k, k'\right) \tag{10}$$

where M_k is the mass of the host atom, and α and β are the directions.

$$\varepsilon = \frac{M_k - M_{k'}}{M_k},$$

where ε is the mass defect parameter, $M_{k'}$ is the mass of a substitutional impurity atom, and $\Delta\phi_{\alpha\beta}\left(k, k'\right)$ arises from the change in the force constant due to the Mn substitution at the Zn site, i.e., $\Delta\phi$ is the force constant difference between Zn–O and Mn–O. Most of the time this is represented by Kellermann's parameters A and B in the form of ΔA and ΔB. With these, $|I - g\partial l|$ is determined for various $x\,(=\omega/\omega_{\max})$ and when the above determinant goes to zero, the x value is noted and hence the LVM is determined. This is given in Table III.

When Mn is considered as a substitutional impurity in ZnO, replacing Zn, the theoretical investigations reveal $502\,\mathrm{cm}^{-1}$ as the localized vibrational mode. This is another reason why the bandgap is affected in nano-ZnO. Apart from exchange interactions, a localized vibrational mode will also interact with the electrons of the host, i.e., the electron–phonon interaction will also contribute in addition to the exchange interaction to change the bandgap.

4. RESULTS AND DISCUSSION

A peak at 390 nm found for nano-ZnO in photoacoustic measurements is compared with 380 nm corresponding to the bulk ZnO. In

general, when the particle size is decreased, a blue shift is expected; otherwise, the PA peak should be below 380 nm. But a red shift is observed here. This can happen in II–VI nanomaterials as reported by Behera et al. [38] due to the presence of excess Zn atoms in ZnO. Behera et al. studied the Raman mode for nano-CdS, where a new mode at 295 cm^{-1} was observed, a red shift. They proposed various possibilities to explain this new mode, such as a surface mode, or a defect mode due to interstitial effects, etc. Finally, they concluded that this red shift to the shoulder is possible when cadmium-rich CdS is grown. So, correspondingly, even in nanomaterials, one can expect a red shift when one metal ion is rich. Indeed, in the present synthesis of nano-ZnO enriched with Zn, the PA did show a red shift (Fig. 5).

The electronic bandgap and the size of the particles are determined from the PA measurements. The size of the particles is 35 nm and the thermal properties of this ZnO nanocrystal are an order of magnitude higher than those for the bulk material, as expected. This is also compared with our earlier results for ZnO nanowire.

The vibrational mode observed from the FTIR spectrum for the doped sample shows a blue shift in contrast to the undoped sample. Because of the size confinement and lattice distortion, not all of the IR absorption modes are fundamental TO modes. The interaction between the electromagnetic radiation and the particles depends on the size, shape, and the state of aggregation of the crystal. Therefore, the difference of the FTIR vibration modes between the bulk and nanoparticles originates from the morphology and size. The undoped and doped samples have more or less the same fundamental modes except for the doped which shows an additional mode at 514 cm^{-1}, which agrees fairly well with the experimental result of Ref. [6] where a mode at 522 cm^{-1} is reported and our theoretical prediction shows a peak at 502 cm^{-1}.

Lattice dynamical investigations were carried out to elucidate the defect modes arising due to the doping of Mn in ZnO. There is no standard theory reported for the defect mode in nanomaterials; therefore, we extended the theory of bulk materials to this nanosystem. In view of the fact that the most commonly used methods are molecular models and Green-function techniques, we carried out these types of calculations for Mn substitution in ZnO. In our molecular model we obtained a defect mode at 463 cm^{-1}, which is not close to the experimentally observed mode at 514 cm^{-1}. This was attributed to the fact that in the molecular model only the central forces and the first neighbors were considered. Therefore, a refined Green-function technique was used to calculate the same localized mode which turned out to be 502 cm^{-1}. This agrees with the present experimental value of 514 and 522 cm^{-1} from Ref. [6]. In Ref. [6]

experiments were carried out for nano-ZnO tetrapods with Mn doping, where the localized mode is $522\,cm^{-1}$. It was concluded that the present nanoparticle treatment of this defect mode is in reasonable agreement with experiment. The theoretical results of the molecular model and the Green-function technique are consistent with our hypothesis that Mn goes as a substitutional defect (displacing Zn) in nano-ZnO.

REFERENCES

1. T. Soki, Y. Hatanaka, and D. C. Look, *Appl. Phys. Lett.* **76**:3257 (2000).
2. P. Sharma, A. Gupta, K. V. Rao, F. J. Owens, R. Sharma, R. Ahuja, J. M. Osorio Guillen, B. Johansson, and G. A. Gehring, *Nature* **2**:673 (2003).
3. T. Dietl, H. Ohno, F. Matsukura, J. Cibert, and D. Ferrand, *Science* **287**:1019 (2000).
4. N. Hasuike, H. Fukumura, H. Harima, K. Kisoda, H. Matsui, H. Saeki, and H. Tabata, *J. Phys.*: *Condens. Matter* **16**:S5807 (2004).
5. U. Ozgur, I. Alivov Ya, C. Liu, A. Teke, M. A. Reshchikov, S. Dooan, Avrutin, S. J. Cho, and H. Morkoc, *J. Appl. Phys.* **98**:041301 (2005).
6. R. Viswanatha, S. Sapra, S. S. Gupta, B. Satpati, P. V. Satyam, B. N. Dev, and D. D. Sarma,*J. Phys. Chem. B* **108**:6303 (2004).
7. L. W. Yang, X. L. Wu, G. S. Huang, T. Qiu, and Y. M. Yang, *J. Appl. Phys.* **97**:014308 (2005).
8. K. J. Kim and Y. R. Park, *Appl. Phys. Lett.* **78**:475 (2001).
9. A. Kaschner, U. Haboeck, M. Strassburg, G. Kaczmarczyk, A. Hoffmann, C. Thomsen, A. Zeuner, H. R. Alves, D. M. Hofmann, and B. K. Meyer, *Appl. Phys. Lett.* **80**:1909 (2002).
10. M. Tzolov, N. Tzenov, D. D. Malinovska, M. Kalitzova, C. Pizzuto, G. Vitali, G. Zollo, and I. Ivanov, *Thin Solid Films* **379**:28 (2000).
11. J. Zuo, C. Y. Xu , L. H. Zhang, B. K. Xu, and R. Wu, *J. Raman Spect.* **32**:979 (2001).
12. C. J. Lee, T. J. Lee, S. C. Lyu, Y. Zhang, H. Ruh, and H. J. Lee, *Appl. Phys. Lett.* **81**:3648 (2002).
13. B. D. Yao, Y. F. Chan, and N. Wang, *Appl. Phys. Lett.* **81**:757 (2002).
14. Z. W. Pan, Z. R. Dai, and Z. L. Wang, *Science* **291**:1947 (2001).
15. M. H. Huang, S. Mao, H. Feick, H. Yan, Y. Y. Wu, H. Kind, E. Webber, R. Russo, and P. D. Yang, *Science* **292**:1897 (2001).
16. J. J. Wua, S. C. Liu, C. F. Wu, K. H. Chen, and L. C. Chen, *Appl. Phys. Lett.* **81**:3648 (2002).
17. W. Gebicki , K. Osuch, C. Jastrzebski, M. Godlewski, and Z. Golacki, E-MRS Spring Meeting. *ZnO and Related Materials*, G-VIII.04 (2005).
18. C. Y. Lee, T. Y. Tseng, S. Y. Li, and P. Lin, *Tamkang J. Sci. Eng.* **6**:127 (2003).
19. A. Rosencwaig, *Phys. Today* **28**:23 (1975).
20. A. Rosencwaig and A. Gresho, *J. Appl. Phys.* **47**:64 (1976).
21. P. Raji, C. Sanjeeviraja and K. Ramachandran, *Cryst. Res. Technol.* **39**:617 (2004).
22. P. Raji, K. K. Umesh, S. Sivakanth, S. K. Ramakrishnan, and K. Ramachandran, *Int. J. Mod. Phys. B* **19**:1 (2005).
23. S. Boggs, J. Kuang, H. Andoh, and S. Nishiwaki, *IEEE Trans. Power Delivery* **15**:2 (2000).
24. J. Horvath, R. Birringer, and H. Gleiter, *Solid State Commun.* **62**:319 (1987).
25. A. J. Kulkarni and M. Zhou, *Appl. Phys. Lett.* **88**:141921 (2006).
26. P. Raji, C. Sanjeeviraja, and K. Ramachandran, *Bull. Mater. Sci.* **28**(3):233 (2005).

27. G. N. Karanikolos, P. Alexandridis, G. Itskos, A. Petrou, and T. J. Mountziaris, *Langmuir* **20**:550 (2004).
28. Y. Jin, B. Zhang, Y. Shuming, Y. Wang, J. Chen, H. Zhang, C. Huang, C. Cao, H. Cao, and R. P. H. Chang, *Solid State Commun.* **119**:409 (2001).
29. L. Brus, *J. Phys. Chem.* **90**:2555 (1990).
30. Y.-L. Du, M.-S. Zhang, and W.-C. Chen, *Chin. Phys. Lett.* **19**:372 (2002).
31. F. Deeremps, J. P. Porres, A. M. Saitta, J. C. Chervin, and A. Polian, *Phys. Rev. B* **65**:092101 (2002).
32. T. C. Damen, S. P. S. Porto, and B. Tell, *Phys. Rev.* **142**:570 (1996).
33. N. Ashkenov, *J. Appl. Phys.* **93**:126 (2003).
34. S. S. Jaswal, *Phys. Rev.* **140**:687 (1965).
35. A. A. Maradudin, E. W. Montroll, G. H. Weiss, and I. P. Ipatova, *Theory of Lattice Dynamics in the Harmonic Approximation*, 2nd Ed. (Academic Press, New York, 1971).
36. P. Plumblle and M. Vandevyuer, *Phys. Status Solid. B* **73**:271 (1976).
37. K. Ramachandran and T. M. Haridasan, *Pramana* **16**:1 (1981).
38. S. N. Behera, S. N. Sahu, and K. K. Nanda, *Indian J. Phys.* **74**(A):81 (2000).